Check for updates

Faceted NiO(111) nanosheets: morphological and catalytic evolution for the oxygen evolution reaction

Elliot Brim, [iD] †[a] Konstantin Kimon Rücker, [iD] †[cd] Dereje Hailu Taffa, [iD] †[d] Darius W. Hayes,†[a] Omeshwari Bisen, [iD] [e] Shaun Alia,[b] Marcel Risch, [iD] [e] Jullian Lorenz, [iD] [c] Corinna Harms,[c] Michael Wark [iD] [d] and Ryan M. Richards [iD] *[ab]

The renaissance of the energy system through the use of green hydrogen by water electrolysis lies behind the development of abundant, active, and scalable catalysts for the oxygen evolution reaction (OER). A fundmental understanding of the surface properties for these materials is of vital importance in producing viable heterogenous catalysts. In this feature article, we summarize several years of collaborative work on a uniquely faceted NiO(111) nanosheet possessing hexagonal holes with a focus on understanding how the evolution of the catalyst surface and bulk composition effects OER performance. The importance of surface faceting, morphological evolution, and metal combination by different doping strategies are all analyzed and summarized to further improve the material's performance. Furthermore, microwave and supercritical synthesis processes are utilized to understand how varying wet-chemical techniques effect the formation of the NiO(111) nanosheet and activity of the material. We discuss our chosen strategies and the difficulties encountered with optimizing a catalyst surface for the OER.

[a] *Department of Chemistry, Colorado School of Mines, 1500 Illinois St, Golden, Colorado 80401, USA. E-mail: rrichard@mines.edu*
[b] *Energy Systems Integration Facility, National Renewable Energy Laboratory, 15013 Denver W Pkwy, Golden, Colorado 80401, USA*
[c] *Institute of Engineering Thermodynamics, German Aerospace Center (DLR), Carl-von-Ossietzky-Str. 15, 26129 Oldenburg, Germany*
[d] *Institute of Chemistry, Chemical Technology I, Carl von Ossietzky University of Oldenburg, Carl-von-Ossietzky-Str. 9-11, 26129 Oldenburg, Germany*
[e] *Nachwuchsgruppe Gestaltung des Sauerstoffentwicklungsmechanismus, Helmholtz-Zentrum Berlin für Materialien und Energie GmbH, Hahn-Meitner-Platz 1, 14109 Berlin, Germany*
† Author contributed at least one first-author publication directly used for this feature article.

Elliot Brim received his BA in Chemistry from the Georgia Institute of Technology and received is PhD in Materials Science from the Colorado School of Mines (2025). His research focused on the synthesis and physical characterization of metal oxides catalysts and their application in renewable energy technologies. His other research interests include exploring sustainable scale-up of green technologies and the logistics and implementation of renewable solutions into a future green economy.

Elliot Brim

Dereje H. Taffa is a senior research associate at the Institute of Chemistry, Carl von Ossietzky University of Oldenburg. He studied Chemistry at Addis Ababa University, Ethiopia, and earned his PhD in Chemistry from the University of Osnabrück, Germany. His research focuses on the synthesis, characterization and application of photo(electro)catalyst materials for energy storage and conversion.

Dereje Hailu Taffa

1. Introduction

The hydrogen economy is a proposed alternative to fossil fuels in the modern energy landscape.[1–3] To bring this technology to a reality, costs for producing green hydrogen *via* water electrolysis must be reduced. Thus, catalysts have to be further developed that are both competitive and cost-effective.[4–7] The largest hurdle in producing H_2 comes from the reaction kinetics of the oxygen evolution reaction (OER) (Fig. 1).[8–11] Many active catalysts have issues that hinder their widespread use for the OER such as those containing platinum group metals, namely IrO_x and RuO_x, or intricately fabricated materials that are difficult to scale.[12–14] One solution to these issues is in the use of earth-abundant catalysts that are produced in simple and scalable manners.[15–17]

Heterogeneous catalysts have served as the basis for innumerable chemical and industrial processes.[18] The study of the evolution of material morphologies provides the opportunity to delve into the inner workings behind the reaction activities.[20–23] The surface of a catalyst imparts core characteristics to any reaction mechanism by governing the binding energy, reaction kinetics, and density of active sites.[24,25] It is therefore a valuable endeavour to identify how different surfaces and their characteristics promote OER activity.

Different synthesis strategies bring distinct advantages to a material. For example, solid-state reaction methods are often simple, classical, and form stable products but struggle in controlling material nano/microstructural properties.[26,27] Wet chemical methods allow for fine tuning of the reaction conditions to target specific material properties but often have difficulties in scale up because of experimental setup or use of dangerous reactants.[28–30] Due to the unique characteristics of synthetic techniques, a thorough understanding of the advantages and limitations of a synthesis method guides future studies on new or alternative avenues of catalyst development.

To avoid the high costs associated with platinum group metal (PGM) catalysts, earth-abundant transition metal oxides are being explored as viable alternatives as OER catalysts.[17,31–33]

Julian Lorenz is a research associate at the German Aerospace Center (DLR), Institute of Engineering Thermodynamics and deputy team leader of a research group in Oldenburg, Germany. Dr Lorenz received his Bachelor and Master of Science degrees from the Carl von Ossietzky University of Oldenburg, where he also completed his PhD in collaboration with the DLR institute on new electrochemical in situ techniques based on scanning electro-

Jullian Lorenz

chemical microscopy to investigate reactive sites on transition metal oxide catalysts for the oxygen evolution reaction. Dr Lorenz has expertise in materials development for various electrocatalytic reactions in energy conversion technologies, in electrode engineering for fuel cell and water electrolysis, and in scanning probe techniques. His research interests include the characterization of electrocatalysts for the oxygen evolution and reduction reaction, the evaluation for alkaline water electrolysis and fuel cell technologies as well as catalyst development for the nitrogen reduction reaction in electrochemical ammonia synthesis.

Michael Wark is a full professor of technical chemistry and the head of the research group of photocatalysis and sustainable feedstock utilization in the Institute of Chemistry at Carl von Ossietzky University Oldenburg. Since 2019 he is additionally the Dean of the faculty of Mathematics and Natural Sciences. He studied chemistry at the University of Bremen, Germany, where he also received his PhD. After Postdoc work at the University of

Michael Wark

Mulhouse (France), the University of Notre Dame (USA) and the Leibniz University of Hanover (Germany) he became a full professor at the Ruhr University Bochum (Germany) in 2011 and at the Carl von Ossietzky University Oldenburg in 2013. His research interests include materials for renewable energy applications (photocatalysts, electrocatalysts, biomass conversion, biochar), micro- and mesoporous structures, ordered mesoporous thin films, and inorganic–organic hybrid structures.

Ryan Richards is a University Distinguished Professor of Chemistry at the Colorado School of Mines. He obtained his BA in chemistry at Michigan State University, his MS at Central Michigan University, and his PhD at Kansas State University. Ryan is a fellow of the Royal Society of Chemistry and the American Chemical Society and holds a joint appointment at the National Renewable Energy Laboratory

Ryan M. Richards

(NREL). He enjoys working at the interface of the fields of renewable energy, nanoscale materials, sustainability, circular economy, catalysis and inorganic chemistry.
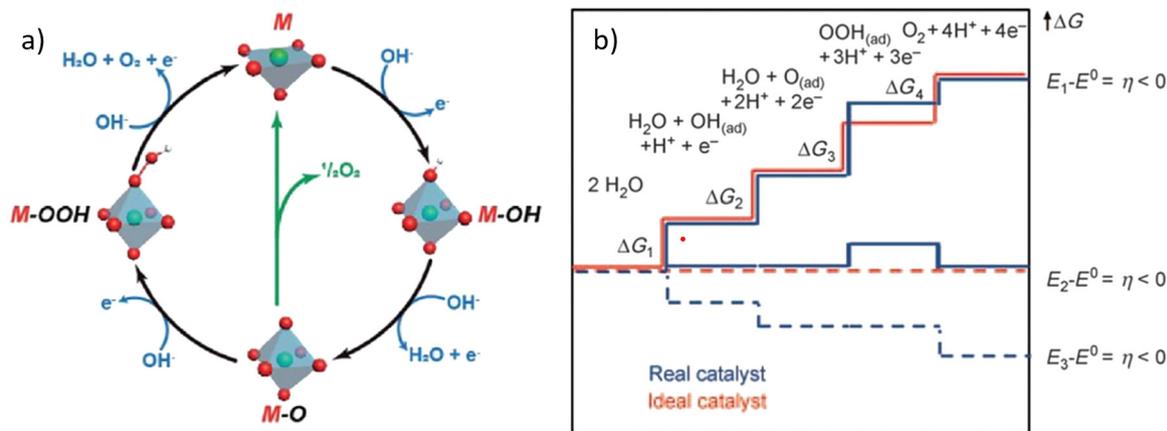
Fig. 1 (a) The OER mechanism of the M–O surface under alkaline conditions. (b) Plot of Gibbs free energy diagram of the OER against the reaction coordination intermediates, reproduced from ref. 19 with permission from *Chem. Sus. Chem*,[19] copyright 2021.

One class of electrolyzers, anion exchange membranes water electrolyzers (AEMWE), promote the use of transition metal catalysts by utilizing an alkaline working environment that heightens their stability.[34–36] Of the extensive list of catalysts tested in the literature, the efficacy of rock-salt structured NiO-based systems for the OER has been well documented, with numerous studies showing competitive overpotentials comparable, if not improved to industry standards.[37–40] The chemical nature of the surface of NiO is a key characteristic of the catalyst by influencing the reaction kinetics through the exposure of the metal centers.[41,42] Lowering the free-energy required for the oxidation of M–O to M–OOH is key to lowering energy costs of electrolysis (Fig. 1).[43]

In this review, we highlight a bottom-up approach of catalyst development on uniquely faceted NiO(111) nanosheets to derive the effect of various physical and chemical changes on the catalyst's OER electrode activity. This project afforded the unique opportunity to pursue a thoroughly fundamental approach to catalyst design, with each step in its development carefully studied and reviewed to understand the underlying changes occurring within the systems. In addition to the fundamental study of catalyst development, two underutilized synthetic methods in supercritical and microwave preparation were explored across and within these studies to determine the reproducibility of the NiO(111) system and understand the unique advantages and similarities between the techniques. Through these evolutions, direct comparisons are drawn between morphology and NiO(111) catalysts' activity for the OER.

2. Preparation of faceted NiO nanosheets

2.1. Principle of faceted materials

The motivation behind the design of a faceted material is the fact that the exposed surface of the catalyst is primarily a controlled chemical environment that imparts specific properties for a desired catalytic purpose.[44–46] There are significant advantages that can be imparted to a catalyst by preferentially

exposing a specific facet on its surface due to promoting a certain chemical scaffolding.[7,47,48] For example, Co_3O_4(001) nanocubes showed higher activities than spheroids due to a change in the active site coordination environment.[49] The synthesis of faceted materials can be challenging due to the delicate balance of thermodynamic stability and controlled crystal growth.[50]

The characterization and confirmation of a surface can be complicated depending on the material analysed. Especially, under OER conditions, the surface structure of transition metal-based catalysts change dynamically requiring the application of *in situ* and *operando* techniques that can trace these changes. Consequently, most synthesized catalyst materials are depicted as 'pre-catalysts' that transform to active phases by surface reconstruction.[51] Facet-dependent transformation processes were studied for example for lanthanum nickelate perovskite thin films showing a mismatch between underlying (001) and (110) facets. The formed NiOOH active surface phase and the (111) surface seemed to favour the formation of 1–2 monolayers of NiOOH, consequently leading to improved OER activity.[52] Some techniques commonly used to identify faceting are the ratio of powder X-ray diffraction pattern (PXRD) peaks, which can reveal a favoured facet compared to an unfaceted material[53] and high-resolution TEM can measure lattice fringes on highly crystalline materials that are characteristic of a specific lattice spacing, or can be used for selected area electron diffraction (SAED) for highly selective diffraction patterns.[54–56] Imaging can also reveal the geometry of the nanomaterial which can then be assessed for faceting.[57,58]

2.2. Preparation methods

Our work has presented the unique opportunity to study the synthesis of a specific catalyst morphology, namely faceted NiO(111) nanosheets with hexagonal holes. The approach is to use analogue synthetic procedures but different preparation techniques and systematic comparison of the results with respect to the synthesis parameters, faceting, and doping. A supercritical synthesis (ST) route uses the unique properties

Table 1 Assessment of synthesis methods for facetted NiO

Method	Advantage	Disadvantage
Solid state	Ease of use	Little control of microstructure
Wet chemical, *e.g.* Pechini	Control of reaction conditions	Scaling, chemical safety
Supercritical synthesis	High diffusion rates, preservation of products	Long reaction time, complex interactions
Microwave-assisted synthesis	Reduced reaction time, selective heating	Non-uniform heating

formed under supercritical conditions to utilize distinct advantages (Table 1).[59,60] The preparation of the reaction media utilizes the qualities of an autoclave-prepared solution-based synthesis up to supercritical conditions.[61] Above this, the supercritical solvent has liquid-like densities but no capillary forces and gas-like compression and mass transport qualities.[62] This allows for a high energy and pressure environment that promotes the solubility of the reactants. Furthermore, the lack of capillary forces means the solvent can be removed from the reaction environment with minimal interaction with any as-prepared products in a technique called supercritical drying.[59] Thus, the as-prepared materials are preserved with the removal of the solvent, preserving any unique micro-structuring and the surface area.

Microwave-assisted synthesis (MW) draws on the efficient heating of reaction media by microwave dielectric heating through the absorption of microwave energy as heat by the reactants and solvent. MW heating is performed primarily through the processes of dipolar polarization and ionic conduction.[63,64] Both methods need the reaction ions interacting at a specific microwave frequency through which heat is generated by molecular friction as the ions oscillate with the electric field. The sum of the heat generated is directly related to the reactions of the media and the electric field. The synthetic advantages afforded through MW synthesis includes significantly reduced reaction times, increased reaction rates, selective heating of the media which promotes selectivity of certain products, and enhanced reaction control (Table 1). These advantages result in MW processes being used for a broad series of electrocatalyst systems, particularly in the OER field.[65–68]

3. Parameters explored

Despite the extensive literature on NiO as a potential OER catalyst, important knowledge gaps remain. The studies discussed in this review aim to advance the understanding of NiO's relationships between catalytic behavior and structure. The first research question explored in this feature article concerns the influence of surface faceting on the OER activity of NiO catalysts. DFT studies previously indicated the activity of the (100) surface of NiO is higher than the (111) surface (Fig. 2).[69] To test this hypothesis, (100) faceted NiO catalysts were synthesized by a molten-salt synthesis and compared to NiO(111) nanosheets.[70] In contrast to the NiO(111) nanosheets, the synthesized NiO(100) catalysts formed as ∼50 nm nanocubes.

This review also seeks to bring together several different studies on NiO(111) nanosheets to bring to light the importance
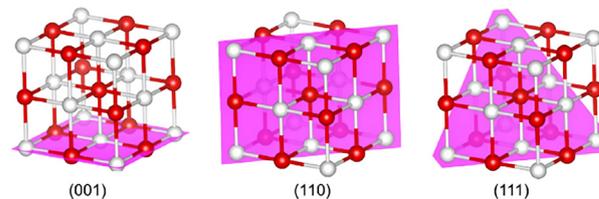

Fig. 2 Low-index atomic planes for the rock salt ($Fm\bar{3}m$) system. The white and red represent the cation and anion respectively, reproduced from ref. 45 with permission from *Cryst. Growth Des.*, copyright 2022.

of morphology, faceting, and preparation methods on catalyst performance. The relationship between nanosheet morphology and OER activity is investigated by varying the calcination temperature of the as-prepared α-Ni(OH)$_2$ nanosheets, producing samples with differing pore sizes and sheet dimensions. The resulting sheets then undergo rigorous electrochemical testing to elucidate any activity differences. Finally, the activity of the NiO catalysts was sought to be improved by the inclusion of dopants into the system, specifically Co and Mn.[71,72] The influence of the Co and Mn dopants on the NiO(111) nanosheet morphology and on the OER activity was studied, finding unique surface reconstruction after doping.[73]

4 Physical changes within the NiO(111) systems

As an additional catalyst reference to the NiO(111) nanosheets and (100) nanocubes, high surface area polycrystalline NiO nanoparticles were also prepared through Li$_2$O reduction (Li$_2$O-MSS). The frameworks of the (111) *vs.* the (100) surfaces differ significantly (Fig. 2). The surface termination of the (100) facet of NiO appears as a checkerboard of Ni and O ions which results in a nonpolar surface plane, and the (110) plane consists of alternating rows or Ni cations and O anions with the same polar character.[74] In contrast, the (111) edge is terminated by an O anion sheet presenting a negatively charged surface.[75] PXRD of the two materials gave the characteristic pattern of the $Fm\bar{3}m$ space group, indicating single-phase rock salt. To corroborate this, X-ray absorption near-edge structure (XANES) and extended X-ray absorption fine structure (EXAFS) determined that the electronic and structural states of NiO(100) nanocubes and NiO(111) nanosheets, despite morphological differences, had Ni K-edge energies with negligible differences indicating that the coordination environments of the bulk were identical. This distinction is critical, as variations in electrochemical behavior are more likely to originate from differences in

morphology or to the bonding environments associated with specific fets. However, NiO(100) had serious agglomeration issues that did not appear in the NiO(111) nanosheets.

Expanding on NiO(111), the nanosheet size, crystallinity, and hole areas are highly affected by the calcination temperature that the precatalyst undergoes. To understand how these differing morphologies effect activity, calcination temperatures were selected ranging from 300 °C to 600 °C. This range was selected because the phase transition from α-Ni(OH)$_2$ to NiO(111) occurs at temperatures above ∼270 °C, and calcining above 600 °C results in the breakdown of the nanosheets into particle agglomerates or rods.[76,77] At higher calcination temperatures, higher crystallinity and lattice contraction are observed.

For both synthetic techniques, the Brunauer–Emmett–Teller (BET) surface area, calculated from N$_2$ desorption isotherms, decreased with the increase in calcination temperature. The inverse was true for crystallite sizes calculated using the Scherrer equation.[78] This is due to the longer reaction times and high reactant mobility of the preparation. This results in decreased surface areas at lower temperatures but better retention of surface area at high temperatures for the ST samples. XPS Ni:O peak ratios were analyzed and both techniques saw an increase in O present (from a Ni:O ratio of 0.97 to 0.85 for MW) as the temperature increased. This is due to the formation of the (111) facet, which is O terminated.[79,80]

To further understand these structural differences, TEM measurements were conducted to observe individual sheet morphologies at different calcination temperatures (Fig. 3). At 300 °C, small pores of random shapes formed within both the MW and ST nanosheets while at 400 °C, well-ordered hexagonal

holes appeared ranging from 10–50 nm in diameter. In the 500 °C materials both ST and MW samples had the same, but larger, hexagonal holes (20–100 nm in diameter). However, the images of MW samples revealed larger, less ordered holes in addition which could be due to separate holes combining during nanosheet annealing. At 600 °C, MW NiO(111) had coarsened to a plate-like structure while the ST maintained the nanosheet shape. In summary, the MW nanosheets have improved surface areas at uncalcined and lower annealing temperatures, but ST nanosheets are more resistant to coarsening at elevated calcination temperatures.

The aforementioned synthesis strategies (ST and MW) offer high flexibility, allowing for the incorporation of various transition metal cations into the NiO host structure. To demonstrate the versatility of these approaches, NiO nanosheets doped with different cations were prepared.[73,81] When discussing the doping of NiO(111), doping levels are denoted as ST/MW-NiO(111) + x% M (M = Co, Mn) and varied between 1% and 10 mol%. Metal contents for all samples were measured by ICP-MS and confirmed the intended concentrations. For the doped samples, all PXRD patterns showed phase pure rock salt space group except for ST-NiO(111) + 10% Mn, which had a separate Mn$_x$O$_y$ phase.[81,82] A shift in the reflex peaks was observed for all doped samples on account of the different cationic radii of the dopants.[37] The ST samples corroborate this semi-quantitatively by average d-spacing measurements acquired through HRTEM. TEM imaging suggested that the samples maintained the nanosheet morphology and contained the characteristic hexagonal holes of the pristine material (Fig. 4b).[83] The Co-doped samples for both MW and ST methods had hole diameters most closely resembling the pristine NiO(111) (10–50 nm)
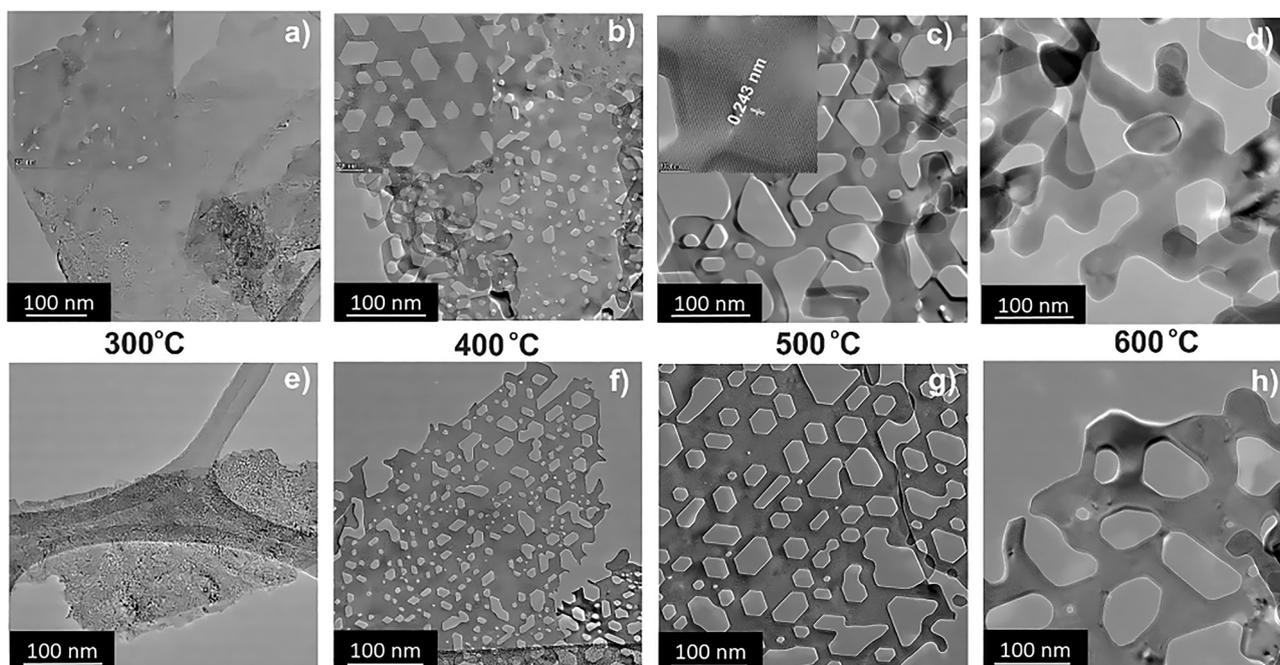

Fig. 3 HR-TEM images (a)–(d) for MW samples and (e)–(h) for ST samples, reproduced from ref. 53 with permission from *ACS Appl. Mater. Interfaces*, copyright 2024.
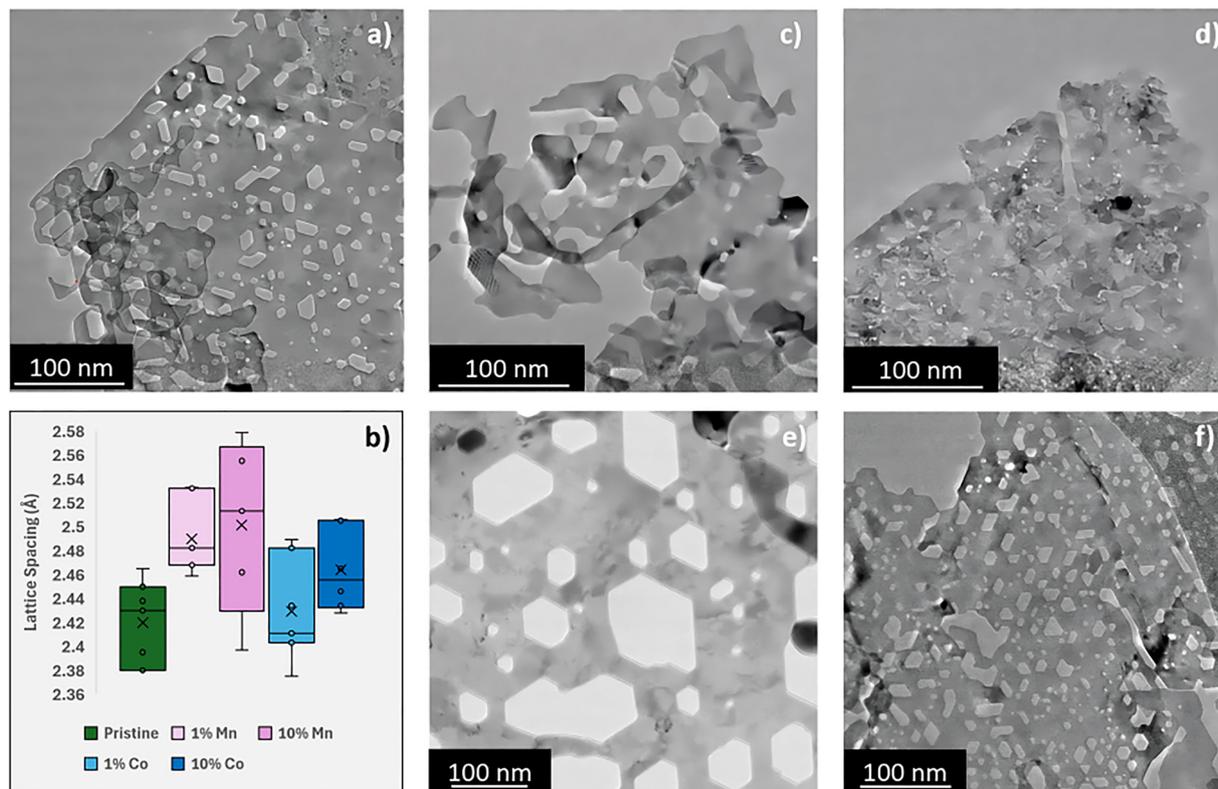
Fig. 4 Transmission electron microscopy images of pristine NiO(111) (a), MW-NiO(111) + 5% Co (c), and + 5% Mn (d). ST-NiO(111) + 5% Co (e) and +5% Mn (f) are included for comparison. (b) Candlestick plot with the average *d*-spacing for ST-NiO doped samples taken over minimum 8 locations, adapted from ref. 73 and 81 with permission from *J Phys. Chem. C & RSC Appl. Interfaces*, copyright 2025.

while Mn-doped samples contained smaller holes (Fig. 4). This is likely due to the larger lattice distortion effect higher valent Mn has on the NiO system.[73,84]

N₂ physisorption showed larger surface areas in Mn samples relative to pristine NiO(111) (calculated by the BET method) but no significant changes in Co doped NiO(111). XAS and XPS experiments were performed before electrochemical cycling to probe the influence of Co and Mn doping on the oxidation state and surface reconstruction.[73] The Ni oxidation state of all samples as determined by the Ni K-edge through X-ray absorption near-edge spectroscopy (XANES) is +2.5. Extended X-ray absorption fine structure spectra (EXAFS) agree with PXRD that the bulk is a rock salt structure. Ni $2p_{3/2}$ spectra for pristine, 5% Co and Mn doped samples indicate minimal change due to dopant inclusion.[73,81]

5. Electrochemical trends of the NiO(111) catalysts

5.1. (111) *vs.* (100) facet activities

The surface and bulk characterization of the various catalysts revealed that while there are significantly different morphologies between the studied materials, the chemical aspects of the NiO(111) catalysts appeared to be identical. Therefore, the differences in any observed OER activity stems from the

physical differences of the catalysts. Rotating disk electrode (RDE) experiments showed there were significant differences in activity between the samples (Fig. 5a). The NiO(100) catalyst mixed with Nafion ionomer exhibited far worse dispersibility in the deionized water/isopropanol solvent mixture compared to NiO(111) which led to worse distribution of the catalyst across the electrode. Li₂O-MSS NiO showed much better dispersion ascribed to reduced agglomeration of the material, but its moderate activity was believed likely due to less access to active sites through residual reactants, still present agglomeration, and poly/reduced crystallinity.

Potentiostatic hold studies at 1.6 V over 2 h showed that NiO(111) maintained a more stable holding current of ∼45 mA cm⁻² over the period. Linear sweep voltammetry (LSV) analysis (Fig. 5a and b) revealed a substantial decrease in both the NiO(100) and Li₂O-MSS NiO potentials in comparison to the NiO(111), with neither reaching the common benchmark of 10 mA cm⁻². So instead, the average current of the catalysts at 1.55 V was found for both samples, with Li₂O-MSS NiO showing currents 8–9 times less and Ni(100) 14–15 times less than NiO(111). In the NiO(100) cyclic voltammograms (CV) there are O₂ reduction peaks visible, which are related to the oxygen reduction reaction. (ORR) activity of the underlying Au substrates due to the insufficient coating process. The results suggests that the lower activity is at least partially resulting from the unoptimized coating process, as
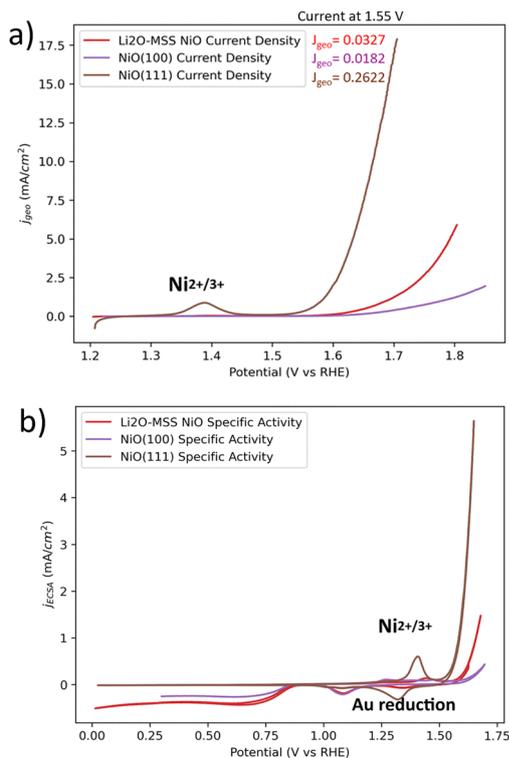
Fig. 5 (a) Linear sweep voltammogram at a scan rate of 10 mV cm^{-1} (top) and cyclic voltammograms (bottom) of Li$_2$O-MSS NiO, NiO(100), and NiO(111) nanomaterials in a non-purified 0.1 M NaOH electrolyte evaluating the trends for the current density. (b) Cyclic voltammograms at 10 mV s^{-1} scan rate.

not all the geometric surface area is likely electrochemically active.

ECSA calculations were assessed by dividing measured double layer capacitance values by the assumed specific capacitance (40 μF cm^{-2}).[70] ECSA referencing the current density counterbalances lower surface areas obtained for NiO(100) and Li$_2$O-MSS NiO samples and thus shows improved apparent activity of both underperforming samples, more noticeably in Li$_2$O-MSS NiO. CVs at 50 mV s^{-1}. A shift in the peak location at 1.4 V, correlating to the Ni$^{2+/3+}$ transition, indicate that the three samples have a difference in the redox kinetics of the reaction.[7] NiO(111) has the strongest Ni$^{2+/3+}$ peak, indicating more accessible surface sites due to enhanced surface restructuring to the active NiOOH intermediate.[85]

The poor performance shown by the NiO(100) samples is in contrast with the aforementioned DFT calculations.[69] The original hypothesis was that the (100) facet would lower overpotentials through lowering the reaction free-energy of the four-electron transfer process, specifically in the OOH intermediate step.[86–88] The findings may reflect differences in real vs simulated space, as the DFT calculations occurred in vacuum along a non-periodic direction and the reaction free-energy calculation assumed a constant applied potential of 1.57 V. Also, the absence of any consideration for the effect the band structure of NiO may have had an effect on the charge transfer kinetics calculations in the DFT calculations.[69,89] However, there was

also agglomeration issues with the (100) catalyst that hindered its coating of the electrode. What is clear is the sharp divergence between a theoretical system and the dynamic environment of an electrocatalytic system.

5.2. Impact of morphology and synthesis technique on OER activity

To further investigate the high OER activity observed for NiO(111) nanosheets in the previous study, catalysts with varying morphologies prepared by both solvothermal (ST) and microwave-assisted (MW) synthesis methods were evaluated using RDE experiments. During a 50-cycle break in step, cyclic voltammograms of the MW and ST NiO(111) catalysts at all temperatures contained two key features: a redox wave at 1.40 V vs. RHE corresponding to the reconstruction process between Ni^{2+}(OH)$_2$ and Ni^{3+}OOH, and a steep increase in current following this redox wave resulting from oxygen evolution in alkaline electrolyte.[38,42,53] As the catalysts were cycled, the Ni$^{2/3+}$ redox peak increased in magnitude indicating the slight conversion of surface rock salt NiO to more reactive and conductive oxy/hydroxides structures.[40,90,91]

The integral anodic charge trend under the Ni$^{2+/3+}$ redox peak for both MW and ST prepared catalysts from CVS (Fig. 6a and c) follows Ni(OH)$_2$ > 300 °C > 400 °C > 500 °C > 600 °C. This corresponds to the accessibility of Ni metal sites and relates well with the observed surface area changes of NiO(111) as calcination temperature increases. The OER activity does not follow the same trend as the anodic charge, indicating that not all Ni sites during the redox processes participate in the OER.[92] The lowest overpotentials for both MW and ST NiO(111) are observed for the 400 °C and 500 °C samples respectively with overpotentials of 405 mV for ST-NiO(111)and 414 mV for MW-NiO(111) needed to reach 10 mA cm^{-2} (Fig. 6b and d). These overpotentials are higher than reported NiO thin film activities but are comparable or lower than previously reported NiO nanoparticle-based OER catalysts.[12,38,42] Interestingly, the activity trend did not follow the BET surface area trend of the catalysts. Both MW and ST Ni(OH)$_2$ and 300 °C-NiO(111) had worse activities despite higher BET areas which is attributed to the reduced crystallinity of the sample surface and the potential presence of organic residues blocking active sites. However, a difference in crystallinity does not easily explain why the best activities result from 400 °C MW-NiO(111) but 500 °C ST-NiO(111). The double layer capacitance measurements used to estimate the ECSA display higher capacitance values for the 400 °C MW-NiO(111) and 500 °C ST-NiO(111), respectively, which partially explains their higher OER electrode activity.

One theory behind this observation is that the activity difference derives from the surface area of the hexagonal holes rather than the sheet itself. Scanning electrochemical microscopy (SECM) was performed on NiO(111) and found that the hole edges are double-bevelled faces terminated by both (100) and (111) facets, and this highly defect (100) basal plane displayed massively promoted theoretical catalytic activity.[69,93] As shown in the TEM images, the well-defined hexagonal holes
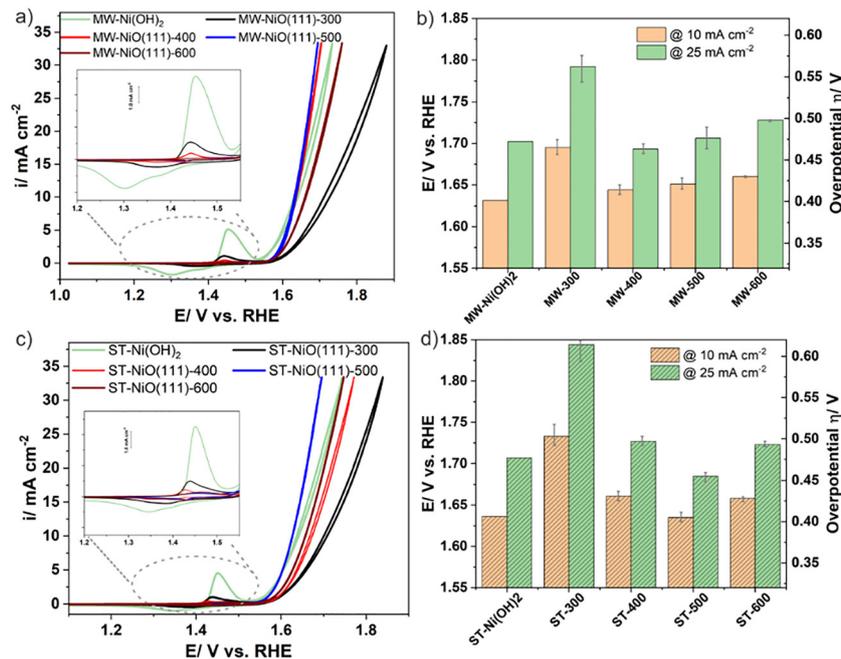
Fig. 6 (a) *iR*-corrected cyclic voltammograms of (a) MW-NiO(111) nanosheets and (c) ST-NiO(111) nanosheets, measured at 10 mV s^{-1} in 0.1 M KOH solution. The insets show the Ni$^{2+/3+}$ redox transitions. Corresponding overpotential comparison at 10 mA cm^{-2} and 25 mA cm^{-2} of (b) MW-NiO(111) nanosheets and (d) ST-NiO(111) nanosheets, reproduced from ref. 53 with permission from *ACS Appl. Mater. Interfaces*, copyright 2024.

in MW NiO at 400 °C have similar diameters and concentrations to those in the ST samples at 500 °C. However, as previously outlined, NiO(100) nanocubes synthesized to further probe this theory had significantly worse activity than NiO(111). So, while the similarities in the morphologies between 400 °C-MW and 500 °C-ST may explain why these are the two samples that show the best activity, the presence of the (100) facet on the hole edge might not account for the activity change. It should be noted that the NiO(100) system was less optimized, and precursor residues may have been a driving reason behind the lack of active sites.

Tafel slope examination agreed with observations in other NiO systems. As current densities increase (for these systems <3 mA cm^{-2} to >5 mA cm^{-2}) there was worse scaling to the higher applied potentials than would be required for application. This has previously been attributed to a change in the OER reaction pathway or the rate-determining step.[93,94] Current densities were normalized to the BET surface area (i_{BET}) and geometric surface area (i_{geo}) at a potential of 1.6V to further understand the activity trends between the two methods. The i_{geo} maxima occurred at the 400 °C-MW and 500 °C-ST samples, and the ST materials generally had higher i_{geo} values at same calcination temperatures. The i_{BET} values for ST catalysts had the same trend as the i_{geo} values but the MW samples kept increasing with calcination temperature. While surface area can be a measure of the number of potential active sites on a catalyst, the actual amount is likely far lower as several sites are inaccessible. Therefore, the loss of surface area through coarsening would be expected to show a loss in activity but is instead changing the accessibility or binding energy of the surface.

When comparing the effects of the two synthesis techniques on the OER activity of the NiO(111) systems, the microwave-synthesized materials exhibited lower overpotentials up to a calcination temperature of 500 °C, beyond which the supercritical (ST) samples showed superior performance. As previously stated, the 400 °C MW and 500 °C ST catalysts shared similarities in crystallinity and morphology, which is why they exhibit the same activities. This shows that the nanosheet morphology plays a significant role as higher surface area NiO(111) had much lower activities. Therefore, the increased crystallinity and formation of the holes within the sheet are important factors to the activity. Furthermore, the sheets lose activity once the materials coarsen into nanoplates/rods and lose the facetted surfaces. Therefore, the formation of the (111) facetted surface and (100) facetted holes play an important role in exposing Ni active sites for the NiO to NiOOH transition.

5.3. Doping contributions to NiO activity

Next, the effect of Co and Mn doping on the OER activity of NiO(111) was investigated to further improve performance. Electrochemical and electrode activity characterization was performed in a 0.1 M KOH electrolyte by a RDE technique. As the activation procedure, the catalysts were cycled 350 times in a potential window from 1.0 to 1.7 V *vs.* RHE at a 100 mV s^{-1} sweep rate to reach stable CVs and promote surface reconstruction. For the ST samples only 5% doping levels were screened while all MW samples synthesized underwent more rigorous electrochemical analysis. Due to this, the MW samples will be discussed in depth in this section while the tested ST samples are simply reported. All samples were calcined at 400 °C to
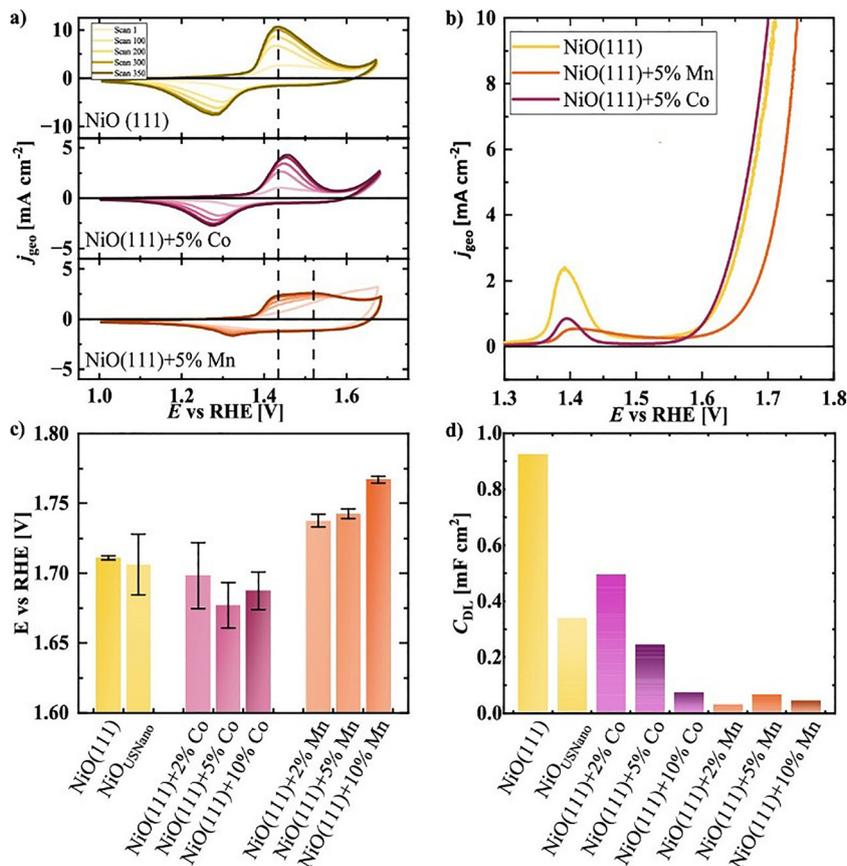
Fig. 7 (a) Representative cyclic voltammograms (CV) of pure NiO(111) and MW-5% Mn- and Co-doped samples with a dotted line at 1.43 and 1.52 V vs. RHE as a visual guide for redox purposes. (b) Positive going linear sweep voltammetry scans of the same materials. (c) Overpotentials at 10 mA cm^{-2} for different doping levels as metric for the OER electrode activity, and (d) double layer capacitance from linear sweep voltammograms at different scan rates, reproduced from ref. 73 with permission from *J. Phys. Chem. C*, copyright 2025.

maintain the characteristic structure of the catalyst. Consecutive CVs and LSVs were developed and analyzed to both compare activity and investigate the structural differences of the materials, and similar peaks to the pristine discussion during activation are seen.[95–98]

The inclusion of the dopants resulted in lower current densities of the Ni^{II}/Ni^{III} redox peak and a shift in position in the CVs (Fig. 7a). This behaviour has been previously reported for Ni-based mixed metal electrocatalysts.[40,87] The features of MW-NiO(111) + 5% Co behave similarly to pristine NiO(111), with the redox peak potential increasing with cycling and little shift in peak position. However, the peak is suppressed which may be a result of inhibited formation of surface NiOOH species (Fig. 7b). No Co$^{2+/3+}$ redox peaks were observed at this doping level indicating that Co is integrating into the NiO surface and forming a mixed-metal surface hydroxide layer.[99]

Voltages with respect to the RHE at 10 mA cm$^{-2}_{geo}$ showed overpotentials with the Co-doped samples of 447 mV for MW-NiO(111) + 5% Co, a decrease of 34 mV compared to pristine NiO(111) (Fig. 7c). Double layer capacitance values do not follow the same trend as overpotentials for the doped materials (Fig. 7d). ST preparation resulted in a worse overpotential at the same doping level of 502 mV which represents an improvement

of 34 mV over the pristine ST-NiO(111). The observed difference in activities between synthesis techniques is likely due to differences in the crystallinity and formation of a well-defined (111)/hole structure as the highest activity calcination temperature of the MW was used.[100] These findings are consistent with comparable studies wereby the inclusion of Co has repeatedly been found to increase the activity of NiO.[7,101,102] Increasing the doping amount of Co above 5 mol% shows no clear trend in activity but slightly increases the overpotential compared to MW-NiO(111) + 5% Co. ECSA has previously been estimated using the surface redox reactions of the catalyst but the application of this method is restricted due to the multiple redox changes present in multi-metal systems.[103] The linear reduction of the specific charge of the Ni$^{2+/3+}$ peak from 231 C g^{-1} to 68 C g^{-1} as Co concentration increases has been previously reported but is not the observed trend in the MW-Co doped materials.[102]

The inclusion of Mn greatly diminishes the activity of the NiO(111) sheets. The best result of MW-NiO(111) + 2% Mn increases the overpotential 37 mV over pristine NiO(111). Upon cycling of the Mn-doped samples, a splitting of the oxidation peak into two overlapping peaks occurs. The peaks have previously been reported for tetrahedral and octahedral spinel

species which may be the result of separate Mn oxidation to MnO_4^- and subsequent leaching processes.[104,105] The leaching of Mn-species was also observed from RRDE ring collector experiments and from ICP-MS of the electrolyte after electrochemistry. Furthermore, cycling of the Mn catalysts resulted in a decrease in activity, which is a trend opposite of that seen in the other materials. The EXAFS data supports strain on the Ni matrix and a change in oxygen stoichiometry as likely explanations of the deviating trend for Mn.[73,104]

Post-cycling XPS spectra revealed shifts in peak intensities with the extent of the $Ni^{2+/3+}$ transformation varying with dopant identity following the trend: pristine > Co > Mn.[40,106] As this is the active surface for the OER process, a suppression in its formation will lower activity. Activity loss in Ni materials by including Mn has been seen previously; e.g. Dionigi et al. performed DFT studies to calculate the surface energies of γ-NiMn LDH and γ-Ni LDH and found that the inclusion of Mn resulted in an increase in the reaction free energy of the OER.[107] Furthermore, these findings suggest that the OER activity and surface reconstruction are not strictly correlated, particularly following the introduction of transition metal dopants into the NiO host.

6. Conclusions

The rational design of catalysts will be a critical enabler for future technologies and utilization of earth-abundant metals and efficient, scalable syntheses are necessary to minimize concerns in catalyst costs. The optimization of catalyst morphology and surface chemistry can be used to push these aspects to the limit. In this feature article, a bottom-up approach was highlighted to elucidate how variations in faceting, morphology, and chemical composition influence the performance of a novel porous NiO(111) nanosheet catalyst for the OER. By systematically cataloguing the structural and compositional factors governing OER activity in Ni-based catalysts, this work provides a unified framework that can guide future catalyst design and development within the broader research community. Additionally, this work highlights both microwave and supercritical syntheses as potential paths forward in electrocatalyst formation and a deeper understanding of these syntheses is achieved through the companion studies performed throughout the research. The increased activity of the nanosheets at high temperatures showed that the formation of the (111) facet and higher crystallinity provided higher performance despite losses in surface area. Furthermore, the doping of NiO(111) with Co and Mn revealed not only activity difference between dopant metals through alterations in surface oxidation pathways but morphological changes as well, as hole areas and sheet shapes change with the selected dopant. Ultimately, this feature highlights that understanding the targeted faceting, focused nanostructure morphology, synthetic process, and chemical surface environment are all critical for optimizing a catalyst system. The findings in this study advance the awareness of these key design factors and aid

in the design for next-generation transition metal oxide water-splitting catalysts. Moving forward, further in-depth exploration of other facets or dopants such as Fe in NiO, or studies mirroring ones shown in this article for other transition metal oxide systems (such as CoO or Fe_2O_3) could further reveal trends between surface chemistry and catalytic activity.[38,99,108]

Author contributions

Brim, E., wrote original draft. Brim, E., Ruecker, K., Taffa, D. H., and Hayes, D. W., wrote first author publications used in this Feature Article. Bisen, O.: Support in synthesis, data curation, software, formal analysis and validation. Alia, S., Risch, M., Lorenz, J., Harms, C., Wark, M.: Project administration, supervision, and resources. Richards, R.: Conceptualization, project administration, and supervision. Paper was reviewed and edited by all authors.

Conflicts of interest

The authors declare no financial or personal conflicts of interest in the work reported in this paper.

Data availability

No new data reported in this manuscript. All data available in the parent articles.

Acknowledgements

Notes and references

1 A. Chaube, A. Chapman, Y. Shigetomi, K. Huff and J. Stubbins, *Energies*, 2020, **13**, 4539.

2 P.-A. Le, V. D. Trung, P. L. Nguyen, T. V. B. Phung, J. Natsuki and T. Natsuki, *RSC Adv.*, 2023, **13**, 28262–28287.

3 A. M. Oliveira, R. R. Beswick and Y. Yan, *Curr. Opin. Chem. Eng.*, 2021, **33**, 100701.

4 M. Grätzel, *Nature*, 2001, **414**, 338–344.

5 H. B. Gray, *Nat. Chem.*, 2009, **1**, 7.

6 M. G. Walter, E. L. Warren, J. R. McKone, S. W. Boettcher, Q. Mi, E. A. Santori and N. S. Lewis, *Chem. Rev.*, 2010, **110**, 6446–6473.

7 D. Hayes, S. Alia, B. Pivovar and R. Richards, *Chem. Catal.*, 2024, **4**, 100905.

8 S. B. Somwanshi, S. B. Somvanshi and P. B. Kharat, *J. Phys.: Conf. Ser.*, 2020, **1644**, 012046.

9 Y. Cheng, F. Kwofie, Z. Chen, R. Zhang, Z. Wang, S. P. Jiang, J. Zheng and H. Tang, *Electrochim. Acta*, 2023, **438**, 141146.

10 D. Pletcher and X. Li, *Int. J. Hydrogen Energy*, 2011, **36**, 15089–15104.

11 H. Dau, C. Limberg, T. Reier, M. Risch, S. Roggan and P. Strasser, *ChemCatChem*, 2010, **2**, 724–761.

12 S. Jung, C. C. L. McCrory, I. M. Ferrer, J. C. Peters and T. F. Jaramillo, *J. Mater. Chem. A*, 2016, **4**, 3068–3076.

13 D. Xu, M. B. Stevens, M. R. Cosby, S. Z. Oener, A. M. Smith, L. J. Enman, K. E. Ayers, C. B. Capuano, J. N. Renner, N. Danilovic, Y. Li, H. Wang, Q. Zhang and S. W. Boettcher, *ACS Catal.*, 2019, **9**, 7–15.

14 S. Park, Y. Shao, J. Liu and Y. Wang, *Energy Environ. Sci.*, 2012, **5**, 9331–9344.

15 F. Song, L. Bai, A. Moysiadou, S. Lee, C. Hu, L. Liardet and X. Hu, *J. Am. Chem. Soc.*, 2018, **140**, 7748–7759.

16 N.-T. Suen, S.-F. Hung, Q. Quan, N. Zhang, Y.-J. Xu and H. M. Chen, *Chem. Soc. Rev.*, 2017, **46**, 337–365.

17 J. Bib Khan and Y.-C. Liang, *Chem. Rec.*, 2024, **24**, e202400151.

18 J. E. Germain, in *Quantum Theory of Chemical Reactions: Chemisorption, Catalysis, Biochemical Reactions*, ed R. Daudel, A. Pullman, L. Salem and A. Veillard, Springer, Netherlands, Dordrecht, 1982, pp. 1–13.

19 T. Wang, W. Wang, W. Shao, M. Bai, M. Zhou, S. Li, T. Ma, L. Ma, C. Cheng and X. Liu, *ChemSusChem*, 2021, **14**, 5112–5134.

20 G. A. Somorjai, *Surf. Sci.*, 1994, **299–300**, 849–866.

21 G. A. Somorjai, *Surf. Sci.*, 1979, **89**, 496–524.

22 G. Ertl, *Angew. Chem., Int. Ed.*, 2008, **47**, 3524–3535.

23 T. Zambelli, J. Wintterlin, J. Trost and G. Ertl, *Science*, 1996, **273**, 1688–1690.

24 J. Hu, K. Zhu, L. Chen, C. Kübel and R. Richards, *J. Phys. Chem. C*, 2007, **111**, 12038–12044.

25 M. A. A. Aziz, A. A. Jalil, S. Wongsakulphasatch and D.-V. N. Vo, *Catal. Sci. Technol.*, 2020, **10**, 35–45.

26 A. Kumar, S. Dutta, S. Kim, T. Kwon, S. S. Patil, N. Kumari, S. Jeevanandham and I. S. Lee, *Chem. Rev.*, 2022, **122**, 12748–12863.

27 B. Parkinson, *Science*, 1995, **270**, 1157–1158.

28 A. Flegler, S. Wintzheimer, M. Schneider, C. Gellermann and K. Mandel, in *Handbook of Nanomaterials for Industrial Applications*, ed. C. Mustansar Hussain, Elsevier, 2018, pp. 137–150.

29 A. V. Nikam, B. L. V. Prasad and A. A. Kulkarni, *CrystEngComm*, 2018, **20**, 5091–5107.

30 A. Gries, F. Langer and J. Schwenzel, *Meet. Abstr.*, 2023, 510.

31 L. Osmieri, J. Park, D. A. Cullen, P. Zelenay, D. J. Myers and K. C. Neyerlin, *Curr. Opin. Electrochem.*, 2021, **25**, 100627.

32 J. Yu, S. Giancola, B. Khezri, D. Nieto-Castro, J. Redondo, F. Schiller, S. Barja, M. C. Spadaro, J. Arbiol, F. A. Garcés-Pineda and J. R. Galán-Mascarós, *EES Catal.*, 2023, **1**, 765–773.

33 D. Xu, M. B. Stevens, M. R. Cosby, S. Z. Oener, A. M. Smith, L. J. Enman, K. E. Ayers, C. B. Capuano, J. N. Renner, N. Danilovic, Y. Li, H. Wang, Q. Zhang and S. W. Boettcher, *ACS Catal.*, 2019, **9**, 7–15.

34 G. F. McLean, T. Niet, S. Prince-Richard and N. Djilali, *Int. J. Hydrogen Energy*, 2002, **27**, 507–526.

35 S. Campagna Zignani, M. L. Faro, A. Carbone, C. Italiano, S. Trocino, G. Monforte and A. S. Aricò, *Electrochim. Acta*, 2022, **413**, 140078.

36 R. R. Raja Sulaiman, W. Y. Wong and K. S. Loh, *Int. J. Energy Res.*, 2022, **46**, 2241–2276.

37 A. Bucci, M. García-Tecedor, S. Corby, R. R. Rao, V. Martin-Diaconescu, F. E. Oropeza, V. A. de la, P. O'Shea, J. R. Durrant, S. Giménez and J. Lloret-Fillol, *J. Mater. Chem. A*, 2021, **9**, 12700–12710.

38 K. Fominykh, J. M. Feckl, J. Sicklinger, M. Döblinger, S. Böcklein, J. Ziegler, L. Peter, J. Rathousky, E.-W. Scheidt, T. Bein and D. Fattakhova-Rohlfing, *Adv. Funct. Mater.*, 2014, **24**, 3123–3129.

39 M.-A. Ha, S. M. Alia, A. G. Norman and E. M. Miller, *ACS Catal.*, 2024, **14**, 17347–17359.

40 L. Trotochaud, J. K. Ranney, K. N. Williams and S. W. Boettcher, *J. Am. Chem. Soc.*, 2012, **134**, 17253–17261.

41 J. Wang, J. Xu, Q. Wang, Z. Liu, X. Zhang, J. Zhang, S. Lei, Y. Li, J. Mu and E.-C. Yang, *Phys. Chem. Chem. Phys.*, 2022, **24**, 6087–6092.

42 H. Radinger, P. Connor, S. Tengeler, R. W. Stark, W. Jaegermann and B. Kaiser, *Chem. Mater.*, 2021, **33**, 8259–8266.

43 J. C. Ehlers, A. A. Feidenhans'l, K. T. Therkildsen and G. O. Larrazábal, *ACS Energy Lett.*, 2023, **8**, 1502–1509.

44 M. Zhu and C. Zhang, *Mater. Lett.*, 2022, **321**, 132409.

45 R. I. Balderas, C. V. Ciobanu and R. M. Richards, *Cryst. Growth Des.*, 2022, **22**, 6296–6322.

46 X. Wang, K. Huang, L. Yuan, S. Li, W. Ma, Z. Liu and S. Feng, *ACS Appl. Mater. Interfaces*, 2018, **10**, 28219–28231.

47 J. Pal and T. Pal, *Nanoscale*, 2015, **7**, 14159–14190.

48 S. Sun, X. Zhang, J. Cui, Q. Yang and S. Liang, *Nanoscale*, 2019, **11**, 15739–15762.

49 Z. Liu, H. M. A. Amin, Y. Peng, M. Corva, R. Pentcheva and K. Tschulik, *Adv. Funct. Mater.*, 2023, **33**, 2210945.

50 L. Aspillaga, D. Jan Bautista, S. N. Daluz, K. Hernandez, J. A. Renta and E. C. R. Lopez, *Eng. Proc.*, 2023, **56**, 22.

51 M. Chen, J. Ma, X. Chen, Q. Liu, Y. Feng and X. Liu, *Chin. Chem. Lett.*, 2025, 111637.

52 A. Füngerlings, M. Wohlgemuth, D. Antipin, E. van der Minne, E. M. Kiens, J. Villalobos, M. Risch, F. Gunkel, R. Pentcheva and C. Baeumer, *Nat. Commun.*, 2023, **14**, 8284.

53 D. H. Taffa, E. Brim, K. K. Rücker, D. Hayes, J. Lorenz, O. Bisen, M. Risch, C. Harms, R. M. Richards and M. Wark, *ACS Appl. Mater. Interfaces*, 2024, **16**, 62142–62154.

54 C. A. Cadigan, A. R. Corpuz, F. Lin, C. M. Caskey, K. B. H. Finch, X. Wang and R. M. Richards, *Catal. Sci. Technol.*, 2013, **3**, 900–911.

55 G. A. Mutch, S. Shulda, A. J. McCue, M. J. Menart, C. V. Ciobanu, C. Ngo, J. A. Anderson, R. M. Richards and D. Vega-Maza, *J. Am. Chem. Soc.*, 2018, **140**, 4736–4742.

56 F. Güder, Y. Yang, A. Menzel, C. Wang, J. Danhof, K. Subannajui, A. Hartel, D. Hiller, R. Kozhummal, N. S. Ramgir, V. Cimalla, U. T. Schwarz and M. Zacharias, *Small*, 2012, **8**, 3307–3314.

57 C. Wang, Z. Huang, Y. Ding, M. Xie, M. Chi and Y. Xia, *J. Am. Chem. Soc.*, 2023, **145**, 2553–2560.

58 W.-Z. Zhang, X.-F. Gu and F.-Z. Dai, *npj Comput. Mater.*, 2016, **2**, 16021.

59 M. Türk, *J. Aerosol Sci.*, 2022, **161**, 105950.

60 G. Brunner, *Annu. Rev. Chem. Biomol. Eng.*, 2010, **1**, 321–342.

61 I. M. Abdulagatov, N. G. Polikhronidi, A. Abdurashidova, S. B. Kiselev and J. F. Ely, *Int. J. Thermophys.*, 2005, **26**, 1327–1368.

62 İ. Şahin, Y. Özbakır, Z. İnönü, Z. Ulker and C. Erkey, *Gels*, 2017, **4**, 3.

63 G. A. Tompsett, W. C. Conner and K. S. Yngvesson, *ChemPhysChem*, 2006, **7**, 296–319.

64 S. Głowniak, B. Szczęśniak, J. Choma and M. Jaroniec, *Adv. Mater.*, 2021, **33**, 2103477.

65 N. E. Sahin, T. W. Napporn, L. Dubau, F. Kadirgan, J.-M. Léger and K. B. Kokoh, *Appl. Catal., B*, 2017, **203**, 72–84.

66 A. Kohlsdorf, D. H. Taffa and M. Wark, *J. Photochem. Photobiol., A*, 2018, **366**, 41–47.

67 A. Martínez-Lázaro, A. P. Mendoza-Camargo, M. H. Rodríguez-Barajas, F. I. Espinosa-Lagunes, Y. Salazar-Lara, A. Herrera-Gomez, O. Cortazar-Martínez, N. Rey-Raap, J. Ledesma-García, A. Arenillas and L. G. Arriaga, *ACS Appl. Energy Mater.*, 2023, **6**, 6410–6418.

68 K. Yan, M. Sheng, X. Sun, C. Song, Z. Cao and Y. Sun, *ACS Appl. Energy Mater.*, 2019, **2**, 1961–1968.

69 T. Sun, D. Wang, M. V. Mirkin, H. Cheng, J.-C. Zheng, R. M. Richards, F. Lin and H. L. Xin, *Proc. Natl. Acad. Sci. U. S. A.*, 2019, **116**, 11618–11623.

70 D. Hayes, E. Brim, K. Ruecker, D. H. Taffa, O. Y. Bisen, M. Risch, S. M. Alia, J. Lorenz, C. Harms, M. Wark and R. M. Richards, *RSC Appl. Interfaces*, 2025, **2**, 1448–1460.

71 Y. Wang, A. Kumar, E. Budiyanto, H. Cheraparambil, C. Weidenthaler and H. Tüysüz, *ACS Appl. Energy Mater.*, 2024, **7**, 3145–3156.

72 T. Priamushko, P. Guggenberger, A. Mautner, J. Lee, R. Ryoo and F. Kleitz, *ACS Appl. Energy Mater.*, 2022, **5**, 13385–13397.

73 K. K. Rücker, D. H. Taffa, O. Bisen, M. Risch, D. Hayes, E. Brim, R. M. Richards, C. Harms, M. Wark and J. Lorenz, *J. Phys. Chem. C*, 2025, **129**, 9341–9355.

74 A. Hermawan, A. T. Hanindriyo, E. R. Ramadhan, Y. Asakura, T. Hasegawa, K. Hongo, M. Inada, R. Maezono and S. Yin, *Inorg. Chem. Front.*, 2020, **7**, 3431–3442.

75 L. Yang, J. Heinlein, C. Hua, R. Gao, S. Hu, L. Pfefferle and Y. He, *Fuel*, 2022, **324**, 124706.

76 K. Chen, W. Li, G. Guo, C. Zhu, W. Wu and L. Yuan, *ACS Omega*, 2022, **7**, 8536–8546.

77 S. H. S. Pai, A. Mondal, R. Barathy, B. Ajitha, J. J. Samuel and Y. A. K. Reddy, *Int. J. Hydrogen Energy*, 2024, **50**, 928–941.

78 P. Scherrer, in *Kolloidchemie Ein Lehrbuch*, ed. R. Zsigmondy, Springer, Berlin, Heidelberg, 1912, pp. 387–409.

79 W. Xing, Y. Zhang, J. Zhu and R. Yu, *Appl. Surf. Sci.*, 2020, **532**, 147427.

80 A. Kerrigan, K. Pande, D. Pingstone, S. A. Cavill, M. Gajdardziska-Josifovska, K. P. McKenna, M. Weinert and V. K. Lazarov, *Appl. Surf. Sci.*, 2022, **596**, 153490.

81 E. Brim, D. Hayes, K. K. Rücker, D. H. Taffa, O. Bisen, M. Risch, S. Alia, J. Lorenz, C. Harms, M. Wark and R. M. Richards, *RSC Appl. Interfaces*, 2025, **2**, 1407–1416.

82 F. Fazlali, A. R. Mahjoub and R. Abazari, *Solid State Sci.*, 2015, **48**, 263–269.

83 J. Hu, K. Zhu, L. Chen, H. Yang, Z. Li, A. Suchopar and R. Richards, *Adv. Mater.*, 2008, **20**, 267–271.

84 M. Gollasch, J. Müller-Hülstede, H. Schmies, D. Schonvogel, P. Wagner, A. Dyck and M. Wark, *Catalysts*, 2021, **11**, 841.

85 M. C. Biesinger, B. P. Payne, A. P. Grosvenor, L. W. M. Lau, A. R. Gerson and R. S. C. Smart, *Appl. Surf. Sci.*, 2011, **257**, 2717–2730.

86 H. B. Tao, Y. Xu, X. Huang, J. Chen, L. Pei, J. Zhang, J. G. Chen and B. Liu, *Joule*, 2019, **3**, 1498–1509.

87 S. S. Jeon, P. W. Kang, M. Klingenhof, H. Lee, F. Dionigi and P. Strasser, *ACS Catal.*, 2023, **13**, 1186–1196.

88 Z. W. Seh, J. Kibsgaard, C. F. Dickens, I. Chorkendorff, J. K. Nørskov and T. F. Jaramillo, *Science*, 2017, **355**, eaad4998.

89 M. Mattinen, J. Schröder, G. D'Acunto, M. Ritala, T. F. Jaramillo, M. B. Stevens and S. F. Bent, *Cell Rep. Phys. Sci.*, 2024, **5**, 102284.

90 S. Haghverdi Khamene, C. van Helvoirt, M. N. Tsampas and M. Creatore, *J. Phys. Chem. C*, 2023, **127**, 22570–22582.

91 B. S. Yeo and A. T. Bell, *J. Phys. Chem. C*, 2012, **116**, 8394–8400.

92 P. Chakthranont, J. Kibsgaard, A. Gallo, J. Park, M. Mitani, D. Sokaras, T. Kroll, R. Sinclair, M. B. Mogensen and T. F. Jaramillo, *ACS Catal.*, 2017, **7**, 5399–5409.

93 R. Poulain, A. Klein and J. Proost, *J. Phys. Chem. C*, 2018, **122**, 22252–22263.

94 D. Antipin and M. Risch, *Electrochem. Sci. Adv.*, 2023, **3**, e2100213.

95 M. Görlin, P. Chernev, J. Ferreira de Araújo, T. Reier, S. Dresp, B. Paul, R. Krähnert, H. Dau and P. Strasser, *J. Am. Chem. Soc.*, 2016, **138**, 5603–5614.

96 R. A. Krivina, Y. Ou, Q. Xu, L. P. Twight, T. N. Stovall and S. W. Boettcher, *Acc. Mater. Res.*, 2021, **2**, 548–558.

97 C. Wang, P. Zhai, M. Xia, W. Liu, J. Gao, L. Sun and J. Hou, *Adv. Mater.*, 2023, **35**, e2209307.

98 H. Bode, K. Dehmelt and J. Witte, *Electrochim. Acta*, 1966, **11**, 1079–1087.

99 Y. Ou, L. P. Twight, B. Samanta, L. Liu, S. Biswas, J. L. Fehrs, N. A. Sagui, J. Villalobos, J. Morales-Santelices, D. Antipin, M. Risch, M. C. Toroker and S. W. Boettcher, *Nat. Commun.*, 2023, **14**, 7688.

100 M. B. Stevens, L. J. Enman, A. S. Batchellor, M. R. Cosby, A. E. Vise, C. D. M. Trang and S. W. Boettcher, *Chem. Mater.*, 2017, **29**, 120–140.

101 A. H. Al-Naggar, V. V. Jadhav, S. F. Shaikh, R. Ali and R. S. Mane, *Energy Fuels*, 2024, **38**, 23699–23712.

102 K. Fominykh, G. C. Tok, P. Zeller, H. Hajiyani, T. Miller, M. Döblinger, R. Pentcheva, T. Bein and D. Fattakhova-Rohlfing, *Adv. Funct. Mater.*, 2017, **27**, 1605121.

103 C. Wei, S. Sun, D. Mandler, X. Wang, S. Z. Qiao and Z. J. Xu, *Chem. Soc. Rev.*, 2019, **48**, 2518–2534.

104 O. Y. Bisen, M. Baumung, M. Tatzel, C. A. Volkert and M. Risch, *Energy Adv.*, 2024, **3**, 504–514.

105 T. Priamushko, R. Guillet-Nicolas, M. Yu, M. Doyle, C. Weidenthaler, H. Tüysüz and F. Kleitz, *ACS Appl. Energy Mater.*, 2020, **3**, 5597–5609.

106 D. Zywitzki, D. H. Taffa, L. Lamkowski, M. Winter, D. Rogalla, M. Wark and A. Devi, *Inorg. Chem.*, 2020, **59**, 10059–10070.

107 F. Dionigi, J. Zhu, Z. Zeng, T. Merzdorf, H. Sarodnik, M. Gliech, L. Pan, W.-X. Li, J. Greeley and P. Strasser, *Angew. Chem., Int. Ed.*, 2021, **60**, 14446–14457.

108 W. Moschkowitsch, N. Zion, H. C. Honig, N. Levy, D. A. Cullen and L. Elbaz, *ACS Catal.*, 2022, **12**, 12162–12169.